Journal of Instrumentation

Study on a compact and adaptable Thomson Spectrometer for laser-initiated $^{11}B(p,\alpha)^{8}Be$ reactions and low-medium energy particle detection

To cite this article: F. Consoli *et al* 2016 *JINST* **11** C05010

Published by IOP Publishing for Sissa Medialab

Received: *March 2, 2016*
Accepted: *April 8, 2016*
Published: *May 11, 2016*

Plasma Physics by Laser and Applications (PPLA 2015)
ENEA Research Centre, Frascati, Italy
5-7 October, 2015

Study on a compact and adaptable Thomson Spectrometer for laser-initiated $^{11}B(p,\alpha)^{8}Be$ reactions and low-medium energy particle detection

F. Consoli,[a,1] **R. De Angelis,**[a] **A. Bonasera,**[b,c] **J. Sura,**[d] **P. Andreoli,**[a] **G. Cristofari,**[a] **M. Cipriani,**[a] **G. Di Giorgio,**[a] **F. Ingenito,**[a] **M. Barbarino,**[c] **C. Labaune,**[e] **C. Baccou,**[e] **S. Depierreux,**[f] **C. Goyon**[e,f] **and V. Yahia**[e]

[a] *ENEA for EUROfusion, Via E. Fermi 45, 00044 Frascati, Italy*
[b] *INFN-LNS, Via S. Sofia 62, 95123 Catania, Italy*
[c] *Cyclotron Institute, Texas A&M University, College Station, Texas 77843, U.S.A.*
[d] *Heavy Ions Laboratory,University of Warsaw, ul. Pasteura 5a, 02-093 Warszawa, Poland*
[e] *LULI, Ecole Polytechnique, CNRS, CEA, UPMC, 91128 Palaiseau, France*
[f] *CEA, DAM, DIF, F-91297 Arpajon, France*

E-mail: fabrizio.consoli@enea.it

Abstract: Thomson Spectrometers are of primary importance in the discrimination of particles produced by laser-plasma interaction, according to their energy and charge-mass ratio. We describe here a detailed study on a set of Thomson Spectrometers, adaptable to different experimental situations, with the aim of being placed directly within the experimental chamber, rather than in additional extensions, in order to increase the solid angle of observation. These instruments are suitable for detection of low-medium energy particles and can be effectively employed in laser-plasma experiments of $^{11}B(p,\alpha)^{8}Be$ fusion. They are provided with permanent magnets, have small dimensions and compact design. In these small configurations electric and magnetic fringing fields play a primary role for particle deflection, and their accurate characterization is required. It was accomplished by means of COMSOL electromagnetic solver coupled to an effective analytical model, very suitable for practical use of the spectrometers. Data from experimental measurements of the magnetic fields have been also used. We describe the application of the spectrometers to an experiment of laser-plasma interaction, coupled to Imaging Plate detectors. Data analysis for spectrum and yield of the detected radiation is discussed in detail.

Keywords: Plasma diagnostics - charged-particle spectroscopy; Spectrometers; Plasma generation (laser-produced, RF, x ray-produced); Erasable phosphors

[1] Corresponding author.

doi:10.1088/1748-0221/11/05/C05010

2016 JINST 11 C05010

Contents

1 Introduction

Laser-plasma interaction generates charged and neutral particles, together with electromagnetic waves ranging from RF-microwaves to γ rays [1]. Particle discrimination is of extreme importance to understand phenomena related to the interaction, but is one of the most difficult type of diagnostics [1, 2]. It can be performed by time-of-flight (TOF) detectors, track detectors (CR-39, PM355...), electrostatic and/or magnetostatic spectrometers [1–4]. TOF-detectors give particle velocity, but supply no information on specie or charge. Track-detectors can count the number of particles and, when used with suitable filters, supply also information on energy and specie [5]. Electrostatic or magnetostatic spectrometers link deflection to particle properties and are very useful when species are known, i.e. to characterize electron beams. When multiple species are present, as common in laser-target experiments, Thomson Spectrometers (TSs) are much more advantageous, since combine both electrostatic and magnetostatic deflection [6, 7]. Incoming particles, selected by a pinhole, draw 2D pictures on the detector plane, from which information on particle energy and charge/mass ratio can be achieved.

Many recent papers deal with definition, characterization and use of TSs for investigating laser-plasmas [7–12]. In general, electrostatic and magnetostatic deflections occur on different stages of the device. The resulting long spectrometers are difficult to adapt to an experimental vacuum chamber normally filled with many objects, and are usually placed in some extensions of it, far from target. This is a main limits for the sensitivity, and for the adaptability of the device to different experimental conditions.

In this work we describe the study on compact spectrometer prototypes thought for low-medium energy particles typical of laser-initiated $^{11}\mathrm{B}(p,\alpha)^{8}\mathrm{Be}$ reactions [13–19]. They induce three-particle

decay [14], either through the ^{8}Be ground state (^{11}B+$p \rightarrow \alpha_0$+^{8}Be, with Q value = 8.59 MeV) or through the ^{8}Be* excited state (^{11}B+$p \rightarrow \alpha_1$+^{8}Be*, Q = 5.65 MeV) and its related decay (^{8}Be$^* \rightarrow 2\alpha_{12}$, Q = 3.028 MeV). The main channel is the second (α_1) and only 1% of reaction products come from the first contribution (α_0). The total fusion cross-section of ^{11}B$(p,\alpha)^8$Be has a high maximum ($\sigma \sim 1.2$ b) associated with a wide resonance at centre-of-mass energy E_{cm} = 660 keV, and a lower resonance ($\sigma \sim 0.25$ b) at E_{cm} = 148.5 keV [18, 20]. Some experiments effectively demonstrated the production of α particles by ^{11}B$(p,\alpha)^8$Be in laser-plasma context [13–19], with a low yield generally expected in these conditions. It is of fundamental importance for the comprehension of these experiments to characterize in details not only possible fusion products, but also proton and boron ions together with all the other species generated in the experiment. This was the main reason to start working on such ion spectrometers.

Peculiar features of the proposed devices are: *simultaneous* electric and magnetic deflection (here achieved by permanent magnets), small and compact structure, tailored shielding against electromagnetic pulses (EMPs). These are fields in the radiofrequency-microwave frequencies, generated by laser-plasma interaction for broad ranges of laser intensity and duration (10^{11}–10^{21} W/cm^2, 10^{-15}–10^{-8} s) [21–24]. They can have frequency spectra up to several gigahertz, duration up to hundreds of nanosecond and very high intensity (up to some MV/m), which is thought to be scaling with the target distance. For these reasons they can heavily affect the electronic equipment present inside and also nearby the experimental chamber. Typically, time-of-flight detectors become blind for a long time interval, and in many cases some devices can be even damaged.

The TSs features allow them to be placed inside the vacuum chamber and to be suitable to many different experimental conditions. On the other hand, this compactness implies short electrode length; thus primary role on particle deflection comes from electric and magnetic field immediately external to the electrode area (*fringing fields*) [10, 25]. Thus, simple equations commonly used for the spectrometer modelling [8, 10, 11, 25] are here not accurate. For this reason we developed an effective analytical model of the structure, coupled to tailored electromagnetic numerical modelling by a commercial solver and to experimental measurements of the magnetic field. In this work we show the successful use of these spectrometers in characterization of ^{11}B$(p,\alpha)^8$Be experiments by laser-target interaction, when coupled to Imaging Plate (IP) detectors [10, 11]. In particular, accurate data analysis for spectrum and yield of the detected particles is discussed in detail.

2 Thomson Spectrometers

2.1 Structure description

Several prototypes of these small and compact spectrometers were designed and realized [26, 27] on the purpose to be suitable to many different experimental conditions. They have scalable Neodymium permanent magnets and simultaneous electrostatic-magnetostatic deflection. The scheme of one of the proposed structures is shown in figure 1 together with two of its realizations, whose parameters are indicated in table 1. Electrodes and magnets have same length and width. A robust iron frame allows the magnets to be fixed in place, despite the mutual repulsive force. Kapton foils are important to isolate electrodes and avoid electrical discharges. The BIG version has been thought for energetic ions up to some tens of MeV, whereas the SMALL one is more suitable for

2016 JINST 11 C05010

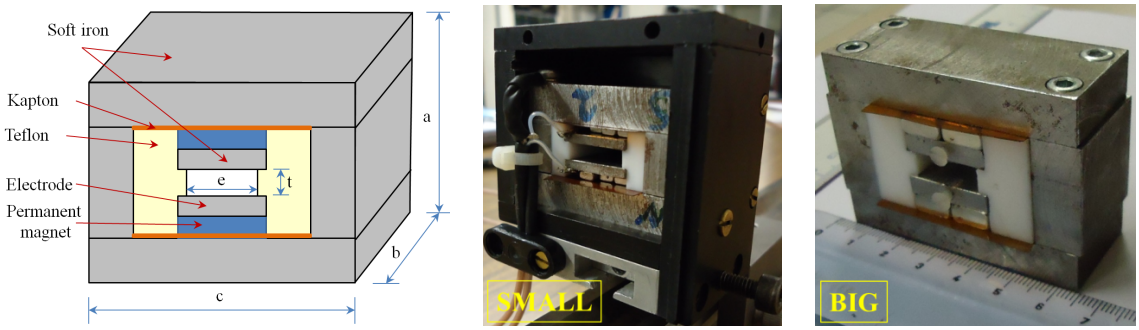

Figure 1. Scheme of one type of the Thomson Spectrometer prototypes [26, 27], together with two of its realizations: the 'SMALL' and the 'BIG' one.

Table 1. Parameters of the Thomson Spectrometers.

	SMALL VERSION	**BIG VERSION**
***a* [mm]**	28	45
***b* [mm]**	16	25
***c* [mm]**	40	60
***t* [mm]**	4	6
***e* [mm]**	13	16
Measured $B_{\perp max}$ [kG]	1.2; 2.1; 2.2; 2.4	4.3
$\Delta V_{\max}$ [kV]	5	9
$E_{\perp max}$ [MV/m]	1.25	1.5

lower energies and its magnetic field is easily scalable. In table 1 measurements of the maximum orthogonal magnetic field, performed by Hall probe, are indicated for some realizations of the two prototypes. One version of the SMALL spectrometer, with magnetic field scaled to be low, was used also as magnetic spectrometer for electrons [27].

In figure 2 it is shown the internal structure of a mounting example of the SMALL spectrometer when used in real experiments. Similar configuration is applied to the usual BIG case. These setups were employed in recent experiments performed at École Polytechnique with LULI2000 and ELFIE laser systems [18, 19], and mounted inside the vacuum chamber, ~ 30 cm far from target. In these conditions protection against X-rays and electromagnetic pulses (EMPs) is a very delicate issue, because both limit the spectrometer sensitivity. X-rays affect the background on the detector (in this case Imaging Plate), and are mainly generated by direct laser-plasma interaction, with important contributions coming also from X-rays emissions by particle bremsstrahlung on chamber surface and on objects spread within it. Suitable Al and lead shields were thus used to limit this effect.

Spectrometer proximity to target makes mitigation of EMP effects important and very delicate, because of the high intensity of expected fields [23, 24]. An ideal protection from EMPs would require a completely-closed conductive shield with thickness enough larger than the skin-depth at the lowest signal harmonics. In common cases the shield may be not enough thick and anyway some holes are always present (e.g. pinholes and electrode connections). Thus EMP fields can enter the spectrometer, and this is known to be one of the main factors producing parabola tracks on the detector plane modulated by some sinusoids [12, 28, 29]. It is particularly detrimental when

2016 JINST 11 C05010

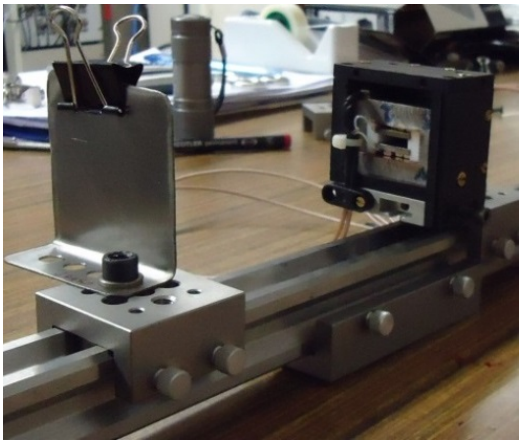

Figure 2. Internal structure of a mounting example of the SMALL Spectrometer, outlining TS, alignment frame and IP holder.

superimposition of different parabolas is produced. The effect mainly occurs when EMP electric field couples with the conductive poles of the active regions, acting as parallel-plate waveguides. The short length of the single stage of deflection in spectrometers here studied greatly attenuate this coupling, compared to common devices with long dual-stages. The choice of permanent magnets reduces external connections. The use of dual power supply for the electrodes, related suitable connections for the ground contacts and general high care on shielding leads to overall high rejection to EMP effects.

2.1.1 Detector

The high level of EMP intensity at small distance from target makes hard and often impossible the use of active detectors as microchannel-plates. The choice of Imaging Plates or CR39 plastic track detectors is thus mandatory. In this work we will present measurement results achieved with BAS-TR and BAS-MS Imaging Plate models, whose properties are in table 2 [30, 31]. The main difference is that BAS-TR has not protective layer, and the sensitive layer has much lower thickness. So it is suitable for low-energy particles. To reduce background due to X-rays, we added to BAS-TR a 3 μm Al filter, directly on the detector plane. The presence of protective layers imposes low-energy thresholds on particles, depending on the species. We calculated them by SRIM simulations (see table 3) [32].

2.2 Modeling

In figure 3, a scheme of the Thomson Spectrometer principle is shown. Usually, modeling of electrostatic and magnetostatic fields in these devices considers them constant within the active regions (here, having b length in figure 1 and 3), neglecting fringing fields [7, 8, 10, 11]. This is not accurate for these compact realizations [9, 25] since these fields play an important role on particle deflection. Thus, suitable modeling of them by COMSOL^{TM}, a commercial electromagnetic numerical solver based on Finite Element Method [33], was here used together with measurements of magnetostatic fields by Hall probe. In figure 4 results of simulated vertical components of fields along the $y-$symmetry-axis (see figure 3) are shown for both SMALL and BIG configurations. Applied voltage is 5 kV and 9 kV respectively. The maximum magnetic field is 2.1 kG and 4.3 kG

2016 JINST 11 C05010

Table 2. Properties of BAS-MS and BAS-TR Fujifilm Imaging Plates [30, 31].

	MS	TR
Protective layer	C_2H_2O	Not present
Density (g/cm^3)	1.66	
Thickness (μm)	9	
Sensitive Layer	$BaFBr_{0.85}I_{0.15}$:Eu	
Density (g/cm^3)	3.31	2.85
Thickness (μm)	115	50
Support Layer	C_2H_2O	
Density (g/cm^3)	1.66	1.66
Thickness (μm)	190	250
Magnetic Layer	$ZnMn_2Fe_5NO_{40}H_{15}C_{10}$	
Density (g/cm^3)	2.77	2.77
Thickness (μm)	160	160

Table 3. Thresholds for BAS-MS and for BAS-TR with 3 μm Al layer, calculated by SRIM [32].

Energy Thresholds	MS [keV]	TR + 3 μm Al [keV]
H	550	300
He	2050	850
B	6500	2300
C	8000	2800

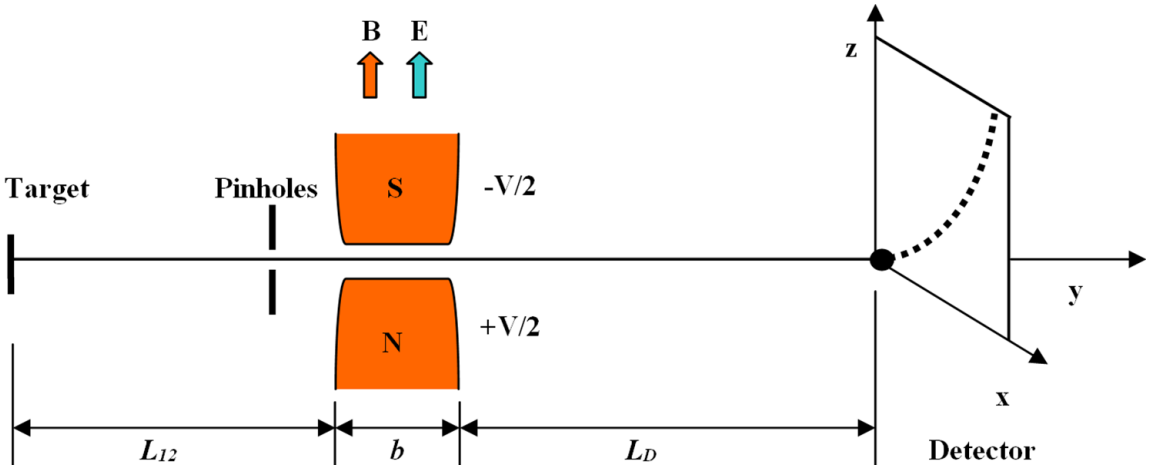

Figure 3. Scheme of the Thomson Spectrometer configuration, with indication of the magnetostatic-electrostatic deflector, drift and detector.

respectively, as from measurements in specific realized prototypes (table 1). Simulations also showed that transversal changes of these profiles can be considered negligible, as far as we use pinholes enough symmetrically centered in the xz plane with respect to electrodes and magnets, and with diameter much lower than t (see figure 1 and table 1).

Particles emitted from target pass through pinholes, are subject to electrostatic-magnetostatic deflection and then continue their motion up to the detector. For each particle, the point of

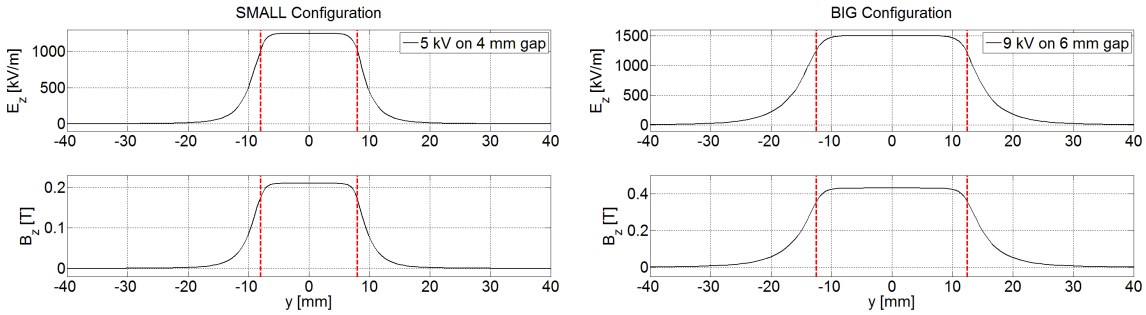

Figure 4. Numerical simulations of vertical electrostatic and magnetostatic fields along the y-symmetry-axis for SMALL and BIG spectrometers. $\Delta V_{\mathrm{SMALL}} = 5\,\mathrm{kV}$; $\Delta V_{\mathrm{BIG}} = 9\,\mathrm{kV}$. Red dashed lines indicate b length of active region in table 1.

interception in the detector plane is indicated with the (x, z) coordinates. From Newton's Second Law, we developed a classical set of equations relating these coordinates to particle properties, but here taking into account the nonuniform fields:

$$x = \frac{q_i}{m_i v_i} A_B \rightarrow \frac{q_i}{\sqrt{2 m_i E_i}} A_B \tag{2.1}$$

$$z = \frac{q_i}{m_i v_i^2} A_E \rightarrow \frac{q_i}{2E_i} A_E \tag{2.2}$$

where q_i, m_i, v_i and E_i are particle charge, mass, velocity and energy, respectively and

$$A_B = \int_0^{L_{12}+b+L_D} \int_0^{y} B_{\perp}(y')\, dy' dy \tag{2.3}$$

$$A_E = \int_0^{L_{12}+b+L_D} \int_0^{y} E_{\perp}(y')\, dy' dy \tag{2.4}$$

are the integral coefficients including the nonuniform fields, where L_{12}, b and L_D are shown in figure 3. For the SMALL spectrometer $L_{12} = 280\,\mathrm{mm}$ and $L_D = 287\,\mathrm{mm}$, and for the BIG one $L_{12} = 345\,\mathrm{mm}$ and $L_D = 322\,\mathrm{mm}$. L_{12} distance defines, together with pinhole diameter, the solid angle covered by the spectrometer and so to its sensitivity, whereas L_D is associated with the optical track enlargement on the detector plane, once L_{12} is fixed. Simulated electric fields, simulated and measured magnetic fields are used to evaluate A_E and A_B. As classical in previous modeling with uniform fields [7, 8, 10, 11], in this way eqs. (2.1–2.2) describe the parabola $z = \left[m_i A_E / \left(q_i A_B^2\right)\right] x^2$, passing from origin and with coefficient dependent on m_i/q_i ratio, and link parabolic coordinates to particle energy. With these equations, information on particles are supplied from parabolas stored on the detector, but it is necessary to know the orientation with respect to the x and z spectrometer axis. This is usually a very delicate issue and requires stable and calibrated configurations. Moreover, when passive detectors are used (Imaging Plates, CR-39) their orientation may vary because of not exact replacement after each experiment. Nevertheless, from eqs. (2.1–2.2) it is possible to determine a very useful formula giving particle energy with respect to $\rho^2 = x^2 + z^2$, i.e. the distance from axes origin:

$$E_i = m_i k^2 \left[1 + \sqrt{1 + \left(\frac{A_E}{k A_B}\right)^2}\right] \tag{2.5}$$

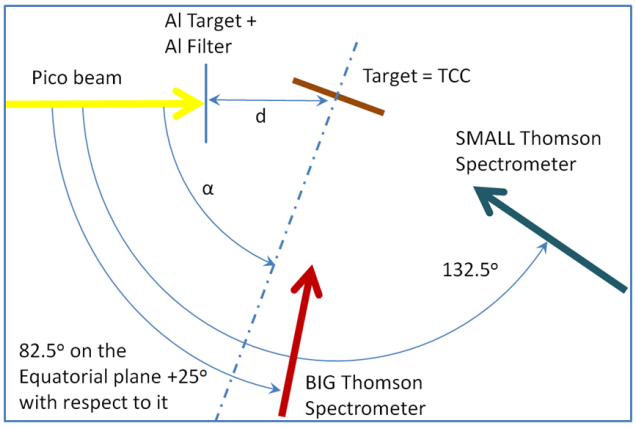

Figure 5. Scheme of the experiment — top view. $d = 1.8\,\text{mm}$ and $\alpha = 70°$. The target at TCC (Target Chamber Center) was natural B.

where $k = q_i A_B / (2 m_i \rho)$. In this case no information on orientation is needed, but it is necessary to make hypothesis on the specific type of particle (i.e. m_i and q_i).

3 Experimental measurements

3.1 Experiment description

We describe here the first use of the SMALL and BIG spectrometers in an experiment on the initiation of $^{11}\text{B}(p,\alpha)^8\text{Be}$ reactions, performed at LULI2000 facility of École Polytechnique [16, 18, 19]. The scheme of the experiment is in figure 5. A laser beam having $\lambda = 527\,\text{nm}$, 1 ps duration and 23 J energy (indicated in figure 5 as the yellow 'Pico beam') was focused with normal incidence on 20 μm Al plain target (with focal position on Al surface) at intensity $\sim 6 \cdot 10^{18}\,\text{W/cm}^2$. The Al target was closely followed by a parallel 10 μm Al foil needed as target protection, because in other shots of the same experimental campaign — here not reported — another laser beam from opposite direction was used [16, 18, 19]. The two Al foils are indicated as a whole in figure 5. We expect that under these conditions TNSA mechanism on first Al foil accelerates fast particles coming from impurities deposited on the rear side of the target [34]. So we should mainly achieve H, C, N, O, Al, ... particles. Those with higher energies are mainly directed along target normal, whereas for smaller energies the emission cone around this normal has increasing angles. Ions then meet the second Al foil, and those with enough energy may reach the natural boron target (consisting of 20% ^{10}B and 80% ^{11}B), interacting with it. As stated in the Introduction, cross-section of $^{11}\text{B}(p,\alpha)^8\text{Be}$ has high resonance at $E_{\text{cm}} = 660\,\text{keV}$ centre-of-mass energy [18, 20], so incoming protons with enough energy may start this reaction, whose products were effectively measured in ref. [16, 18] by tracks on CR39, with low yield.

A SMALL spectrometer was placed on the equatorial plane (see figure 5), equipped with 0.2 mm conical pinhole and BAS-TR detector with 3 μm Al protection. A BIG spectrometer was at +25° with respect to equatorial plane, with 1 mm conical pinhole and BAS-MS plate. Fujifilm FLA7000 scanner was used to retrieve data from IPs and conversion formula from greyscale levels to PSL (PhotoStimulated Luminescence counts) was used [11]. The use of Thomson Spectrometers

2016 JINST 11 C05010

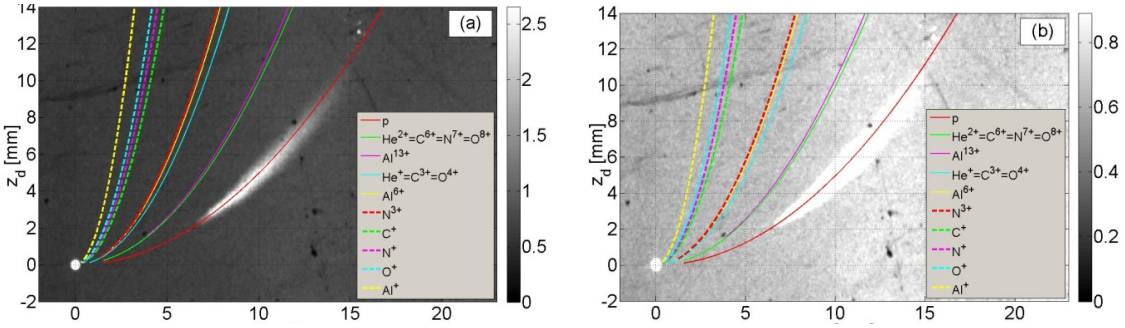

Figure 6. PSL image produced on BAS-TR +3 μm Al by SMALL spectrometer in different PSL scales and with superimposition of parabolas computed by eqs. (2.1–2.4).

is here devoted to the characterization of all ions involved in this experiment, and potentially also to possible fusion products, in case of yield higher than in cases described in ref. [16, 18].

3.2 Data analysis

We show in figure 6 the PSL image produced on BAS-TR by the SMALL spectrometer fed with 5 kV and having 2.1 kG maximum B field, as in figure 4. The circle at $(0, 0)$ coordinates is the pinhole image on detector due to X-rays from target. Only one parabola track is detected. We superimposed to the experimental image parabolas computed using eqs. (2.1–2.4) for some possible species and a very good fitting was obtained for protons, as expected. The intensity changes along the experimental trace, and with this choice of PSL scale the parabola thickness is rather close to the pinhole-image diameter. Indeed, IP sensitivity and dynamics are very high, and in figure 6b we show the same figure 6a with a different PSL scale. Now the trace has intensity much more saturated and it is much enlarged versus the upper extreme, corresponding to lower proton energies. However, this is a second-order effect, visible when PSL scale approaches the minimum value, which should be expected since ion scattering on pinhole edges and space-charge effects produce more beam enlargement on the detector plane for particles with lower energies. It is apparent that there is good separation of proton track, having $A/Z = 1$ (A = mass number, Z = charge state) from the closest trace $A/Z = 2$, even in the enlarged case of figure 6b.

To determine the total number of particles, we defined a curved domain Ψ horizontally contained within two blue curves (see figure 7a), enough larger than the trace, to include some background. Black dots, grey traces and stains on IP image are the result of small holes on the Al cover and residual X-ray contribution, and a procedure of adaptive background subtraction took care of them. For each fixed z-coordinate the PSL-background was estimated in correspondence of each blue curve. The resulting two PSL values were averaged and this value was considered constant for any pixel within Ψ at that z-coordinate. Thus, we multiplied it for the total number of pixels at that coordinate, obtaining a $Background(z)$ integrated function. For a particle of known charge (proton, in this case) z is related to energy by eq. (2.2). Thus, the final $Background(E_p)$ function (where E_p is the proton energy) is shown with the red curve in figure 7b.

To determine the spectrum quantitatively, we horizontally-added the PSLs values for those pixels in Ψ at fixed z, obtaining the blue curve $Integral(E_p)$ in figure 7b as function of proton

2016 JINST 11 C05010

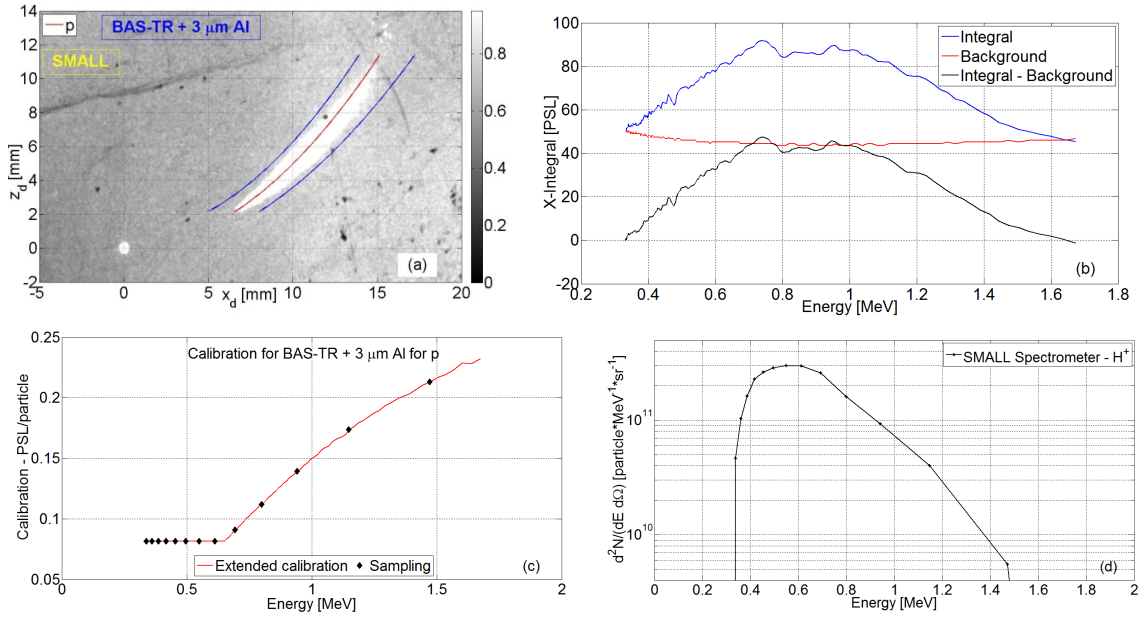

Figure 7. (a) PSL image produced on IP by SMALL spectrometer; (b) PSL integration along x-coordinate for given z, with adaptive background estimation and subtraction. (c) Extended and sampled calibration from ref. [30]; (d) final spectrum for protons.

energy (by using eq. (2.2)). The black curve in the same picture is the function $Integral_{BG}(E_p) = Integral(E_p) - Background(E_p)$, so the total number of PSLs versus energy after the background subtraction. The device resolution depends on pinhole, and in particular on the diameter D_p of its image on the detector plane (circle at (0,0) coordinates). Since eq. (2.2) is nonlinear, the energy intervals $[E_{p\text{-min}}(i) E_{p\text{-max}}(i)]$ (with i interval index) associated with D_p have decreasing width along the proton trace. We define

$$E_{p\text{-}s}\,(i) \equiv \langle E_p \rangle_{[E_{p\text{-min}}(i)\,E_{p\text{-max}}(i)]} \tag{3.1}$$

and

$$\mathrm{Int}_{p\text{-}s}\,(i) \equiv \langle \mathrm{Integral}_{\mathrm{BG}} \rangle_{[E_{p\text{-min}}(i)\,E_{p\text{-max}}(i)]} \tag{3.2}$$

as the sets of averaged proton-energies and PSL-integrals associated with each interval, respectively. IP calibrations supplying the number of PSL per single proton are available in a given energy range [30]. We determined the particle spectrum from the total number of PSLs by adapting those calibrations for protons to the case of their deceleration caused by 3 μm of Al. Unfortunately the calibrations did not cover enough our low energy range and we extended them conservatively as a constant. In figure 7c the extended calibration is shown, together with energy sampling (at $E_{p\text{-}s}(i)$ energies) due to pinhole resolution. The resulting proton spectrum, shown in figure 7d for $E_{p\text{-}s}\,(i)$ energies, is obtained by dividing $\mathrm{Int}_{p\text{-}s}\,(i)$ for the sampled calibrations in figure 7c and for the $4.0 \cdot 10^{-7}$ sr solid angle covered by the pinhole. It is apparent that it has a sharp lower threshold around 300 keV which is in very good agreement with the expected energy cut-off of the 3 μm Al, indicated in table 3. This gives an indication of the good accuracy of results. High-energy cut-off is $\sim$ 1.5 MeV. The total number of particles and those per steradian are indicated in table 4.

2016 JINST 11 C05010

Table 4. Total number of protons through the pinhole and per solid angle for the two spectrometers.

Number of protons	SMALL Spectrometer	BIG Spectrometer
through the pinhole	$5.91 \cdot 10^4$	$2.31 \cdot 10^3$
per solid angle [sr^{-1}]	$1.47 \cdot 10^{11}$	$3.51 \cdot 10^8$

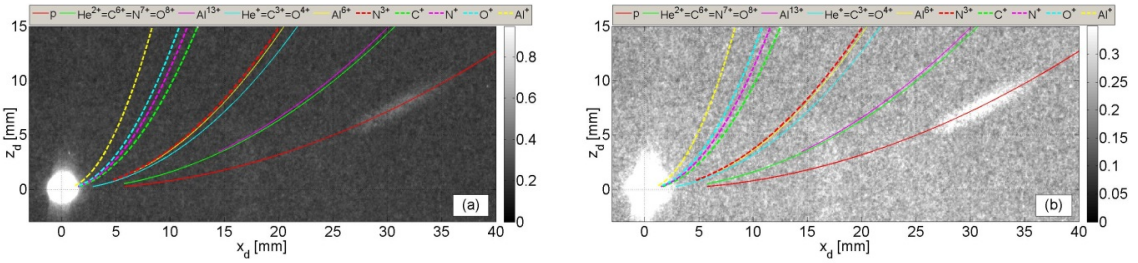

Figure 8. PSL image produced on BAS-MS by BIG spectrometer in different PSL scales and with superimposition of parabolas computed by eqs. (2.1–2.4).

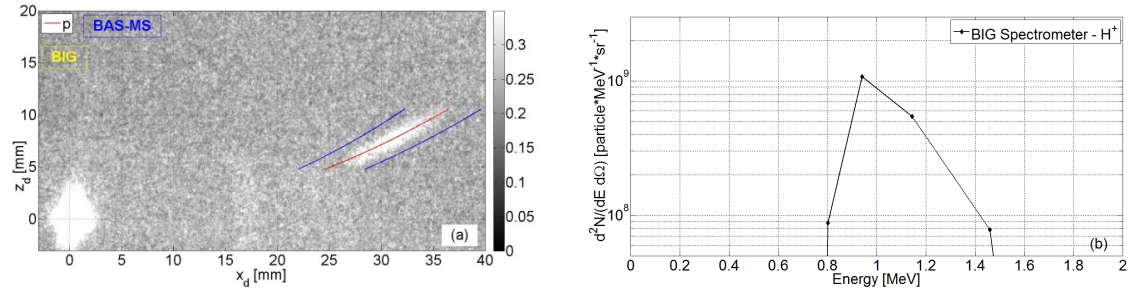

Figure 9. (a) PSL image produced on BAS-MS by BIG spectrometer and Ψ selection by blue curves; (b) final spectrum for protons.

We show in figure 8a-b the PSL image produced on BAS-MS by BIG spectrometer fed with 9 kV and having 0.43 kG maximum B field (table 1 and figure 4). Again only one trace was detected, with good fitting to calculated red parabola for protons, and good separation to the others. Trace intensity was much lower than for the other spectrometer. For a better visualization, in figure 8b we had to improve the image contrast; for this reason the pinhole image at axes origin appears blurry. We applied the same procedure described before for the SMALL spectrometer, and we show in figure 9a the curves defining the Ψ domain. Final proton spectrum is shown in figure 9b and total proton numbers are given in table 4. The large pinhole gave associated solid angle of $6.6 \cdot 10^{-6}$ sr, leading to very good overall sensitivity — higher than for the SMALL spectrometer - and estimated lower-threshold density $E_{\mathrm{LT-BIG-P}} \sim 8 \cdot 10^7$ particles $\mathrm{MeV}^{-1}\ \mathrm{sr}^{-1}$ for protons (figure 9b). Anyway, this decreased the resolution, inevitable drawback when high sensitivity is required [35]. Future trade-off conditions may be chosen depending on the case. High-energy cut-off is ~ 1.5 MeV, in good agreement with data from SMALL spectrometer; but low-energy one is ~ 800 keV, whereas the expected was ~ 600 keV (table 3). We think that this difference could be easily explained considering both spectrometer low energy-resolution and low intensity of the trace with respect to background.

2016 JINST 11 C05010

No sinusoidal modulation of parabolas is observed in these first measurements, sign of EMP effective rejection. Particle yield is much higher for the SMALL spectrometer. This could be explained with its position closer to the Al foil normal, where more particles at high energies are generated. According to TNSA, particles are expected at lower energies when moving far from target normal, but in this case the energy filtering by the 10 μm Al foil and the 9 μm plastic cover of BAS-MS plate have reasonably stopped them. The high sensitivity of Imaging Plates allowed to both spectrometers a good dynamics, also for the case of very low number of particles (BIG case). We were not able to detect traces for $A/Z \neq 1$ parabolas, corresponding to He, B, C, N, O, Al, ... reasonable species. These possible particle flows had energies lower than thresholds required for the detectors and for passing through the 10 μm Al foil, or their number was lower than the E_{LT} spectrometer sensitivity. In particular, in this experiment expected He^{+1} and He^{+2} number of particles per solid angle — taking into account their different (and less intense) PSL calibrations with respect to that for protons [36] — resulted at least two orders of magnitude lower [16, 19] than the estimated BIG spectrometer sensitivity. For future experiments, this can be further improved by decreasing the background level. Moreover, the increasing of the solid angle of observation would certainly help in this sense but at expenses of energy resolution, how seen in figure 7b [35], and with possibility for trace superimposition. Nevertheless, in the present experiment the spectrometers were able to supply precise characterization, at two different angles of emission, of proton beam generated by TNSA and responsible of the $^{11}\mathrm{B}(p,\alpha)^{8}\mathrm{Be}$ reactions, important for the experiment comprehension and quantitative modelling. Remarkable resolution in the proton spectrum by the SMALL device was achieved thanks to the little pinhole.

4 Improved prototypes

To increase the spectrometer sensitivity, we improved the BIG configuration to reduce X-ray contaminations of the detector response. In figure 10 we show a structure mounted within a thick Al cylinder, lead-shielded on the side facing the target, and equipped with two concentric pinholes. General protection against X-rays was enhanced with respect to past prototypes. We believe that important X-ray contribution may come from electrons able to enter the spectrometer, easily deflected by static fields on the internal surface of the Al shield, with important bremsstrahlung illumination of the detector. The two-pinhole configuration, outlined in the scheme of figure 10b, deals with it. A weak magnet is placed just outside the first large pinhole (P1) and practically affects only low-medium energy electrons, deflected so to not enter the second smaller pinhole (P2) and interacting at most with the region between the two pinholes (P1 and P2). In figure 10c the picture of a realized prototype is shown. Effective shielding and grounding are visible.

5 Conclusions

We have described the main features of compact Thomson Spectrometers thought to be used for the study of processes with low-medium energy particles, and specifically for laser-initiated $^{11}\mathrm{B}(p,\alpha)^{8}\mathrm{Be}$ interactions. High sensitivity is required, and for this reason they are put as close as possible to target. Thus, tailored solutions against X-rays and EMPs were necessary. The use of passive Imaging Plates detectors improved EMP immunity and enhanced device sensitivity.

2016 JINST 11 C05010

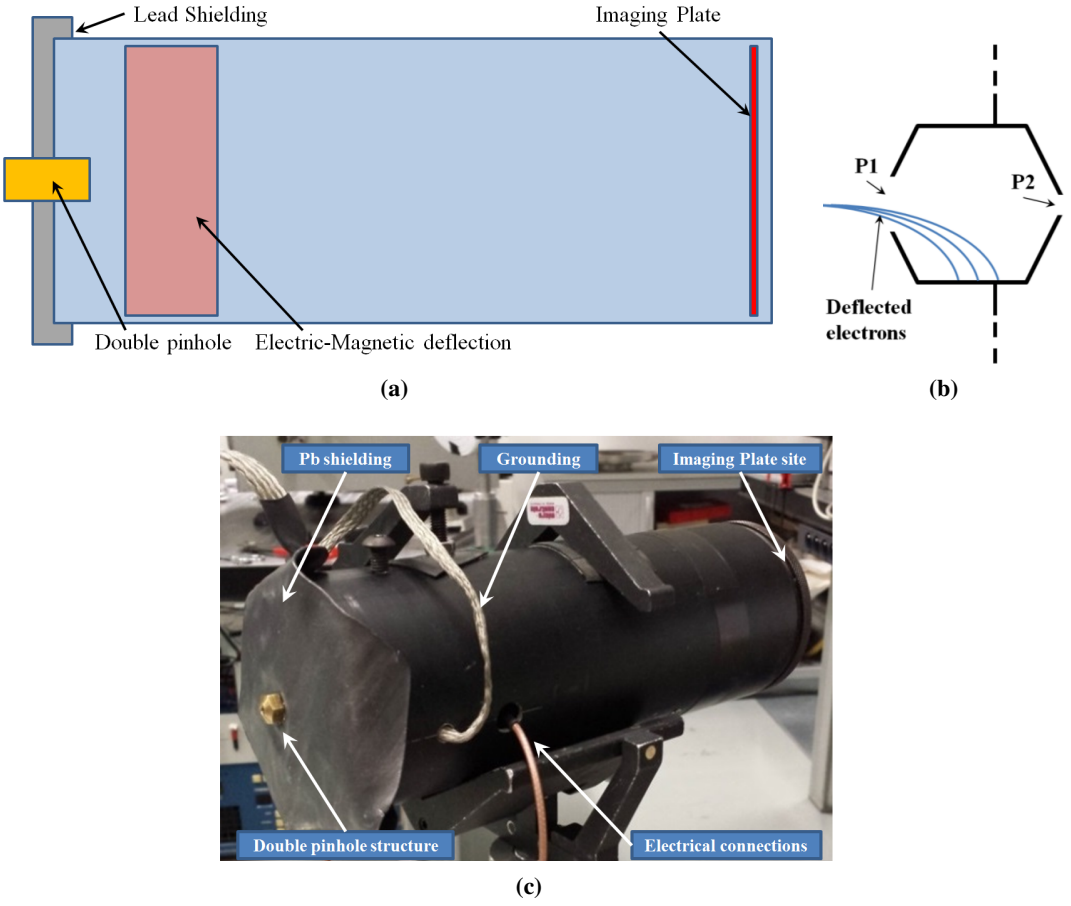

Figure 10. Prototype of the BIG spectrometer with improved X-ray background mitigation. (a) Principle scheme; (b) scheme of the double-pinhole structure; (c) picture of a realized prototype.

The total deflection of these compact structures is highly affected by electric-magnetic fringing fields, and this required numerical simulations, experimental measurements and effective analytical modelling of fields and particle deflection. We showed the first experimental results achieved with two prototypes of these spectrometers, when a proton beam generated by TNSA on thin Al foil interacted with B target. An adaptive process of background subtraction was conceived and applied to detector measurements. This is very important to exploit the high sensitivity and dynamics of Imaging Plates for low particle fluxes in laser-plasma context, locus of intense X-ray emissions. Quantitative spectroscopic description of the generated proton beam was achieved at different angles of emission, important for the experiment comprehension and quantitative modelling. High resolution was obtained with the SMALL spectrometer and high sensitivity with the BIG one. For both devices results were compatible with theoretical expectations. We were not able to detect parabola traces for He^{+1} and He^{+2} and in general for $A/Z \neq 1$ because of energy thresholds and possible number of particles lower than spectrometer sensitivity. Apart from increasing the solid angle of observation, which decreases energy resolution and can produce trace superimposition, this can be further amplified by background lowering. Some spectrometer prototypes have been already improved in this sense and will be tested in future experiments.

2016 JINST 11 C05010

Acknowledgments

This work has been carried out within the framework of the EUROfusion Consortium and has received funding from the Euratom research and training programme 2014–2018 under grant agreement No 633053. The views and opinions expressed herein do not necessarily reflect those of the European Commission.

This work has been partially funded by ENEA contract 05/58/115/AA to Università degli Studi "KORE" di Enna.

References

[1] W.L. Kruer, *The Physics of Laser Plasma Interactions*, Westview Press, Oxford, 2003.

[2] N.G. Basov et al., *Heating and compression of thermonuclear targets by laser beams*, Cambridge University Press, Cambridge, 1986.

[3] G. Münzenberg, *Development of mass spectrometers from Thomson and Aston to present*, *Int. J. Mass Spectrom.* **349-350** (2013) 9.

[4] P.R. Bolton et al., *Instrumentation for diagnostics and control of laser-accelerated proton (ion) beams*, *Phys. Medica* **70** (2014) 255.

[5] R.M. Cassou and V. Benton, *Properties and applications of CR-39 polymeric nuclear track detector*, *Nucl. Track Detection* **2** (1978) 173.

[6] J.J. Thomson, *Rays of positive electricity*, *Proc. R. Soc.* **A89** (1913) 1.

[7] J. N. Olsen et al., *Ion-expansion energy spectra correlated to laser plasma parameters*, *J. Appl. Phys.* **44** (1973) 2275.

[8] D.C. Carroll et al., *A modified Thomson parabola spectrometer for high resolution multi-MeV ion measurements — Application to laser-driven ion acceleration*, *Nucl. Instrum. Meth.* **A 620** (2010) 23.

[9] J.A. Cobble et al., *High-resolution Thomson parabola for ion analysis*, *Rev. Sci. Instrum.* **82** (2011) 113404.

[10] J.T. Morrison et al., *Design of and data reduction from compact Thomson parabola spectrometers*, *Rev. Sci. Instrum.* **82** (2011) 033506.

[11] A. Alejo et al., *Characterisation of deuterium spectra from laser driven multi-species sources by employing differentially filtered image plate detectors in Thomson spectrometers*, *Rev. Sci. Instrum.* **85** (2014) 093303.

[12] G.A.P. Cirrone et al., *A new Thomson Spectrometer for high energy laser-driven beams diagnostic*, 2014 *JINST* **9** T08001.

[13] V. S. Belyaev et al., *Observation of neutronless fusion reactions in picosecond laser plasmas*, *Phys. Rev.* **E 72** (2005) 026406.

[14] S. Kimura, A. Anzalone and A. Bonasera, *Comment on "Observation of neutronless fusion reactions in picosecond laser plasmas"*, *Phys. Rev.* **E 79** (2009) 038401.

[15] A. Bonasera et al., *Measuring the astrophysical S-factor in plasmas*, in *Proceedings of the Fourth International Conference on Fission and Properties of Neutron-Rich Nuclei*, November, 11–17, 2007, Sanibel Island, U.S.A., World Scientific Publishing, Singapore, 2008, pp. 503–507.

2016 JINST 11 C05010

[16] C. Labaune et al., *Fusion reactions initiated by laser-accelerated particle beams in a laser-produced plasma*, Nat. Commun. **4** (2013) 2506.

[17] A. Picciotto et al., *Boron-Proton Nuclear-Fusion Enhancement Induced in Boron-Doped Silicon Targets by Low-Contrast Pulsed Laser*, Phys. Rev. **X 4** (2014) 031030.

[18] C. Baccou et al., *New scheme to produce aneutronic fusion reactions by laser-accelerated ions*, Laser Part. Beams **33** (2015) 117.

[19] C. Baccou et al., *CR-39 track detector calibration for H, He, and C ions from 0.1-0.5 MeV up to 5 MeV for laser-induced nuclear fusion product identification*, Rev. Sci. Instrum. **86** (2015) 083307.

[20] W.M. Nevins and R. Swain, *The thermonuclear fusion rate coefficient for p-^{11}B reactions*, Nucl. Fusion **40** (2000) 865.

[21] F. Consoli et al., *Experiments on Electromagnetic Pulse (EMP) generated by laser-plasma interaction in nanosecond regime*, Proceedings of the 15th IEEE International Conference on Environment and Electrical Engineering (EEEIC), June, 10-13, 2015, Rome, Italy, p. 182 [ISBN: 978-1-4799-7992-9].

[22] F. Consoli et al., *Measurement of the radiofrequency-microwave pulse produced in experiments of laser-plasma interaction in the ABC laser facility,* Physics Procedia **62** (2015) 11.

[23] A. Poyé et al., *Dynamic model of target charging by short laser pulse interactions*, Phys. Rev. **E 92** (2015) 043107.

[24] C.G. Brown Jr. et al., *Assessment and Mitigation of Electromagnetic Pulse (EMP) Impacts at Short-pulse Laser Facilities*, J. Phys. Conf. Ser. **244** (2010) 032001.

[25] M.J. Rhee, *Compact Thomson spectrometer*, Rev. Sci. Instrum. **55** (1984) 1229.

[26] J. Sura, *The Thomson Parabola Spectrometer of the ABC facility*, Internal Report ENEA, Frascati, 2005, unpublished.

[27] F. Consoli et al., *Diagnostics improvement in the ABC facility and preliminary tests on laser interaction with light-atom clusters and p-^{11}B targets*, Nucl. Instrum. Meth. **A 720** (2013) 149.

[28] S. Ter-Avetisyan et al., *Ion diagnostics for laser plasma experiments*, Nucl. Instrum. Meth. **A 623** (2010) 709.

[29] G.A.P. Cirrone et al., *Measurements with an innovative high energy resolution Thomson Parabola Spectrometer*, in *Proceedings of the 40th EPS Conference on Plasma Physics (EPS 2013)*, July, 1-5, 2013, Espoo, Finland, P4.207 [ISBN: 978-163266310-8].

[30] T. Bonnet et al., *Response functions of Fuji imaging plates to monoenergetic protons in the energy range 0.6–3.2 MeV*, Rev. Sci. Instr. **84** (2013) 013508.

[31] G. Boutoux et al., *Validation of modelled Imaging Plates sensitivity to 1-100 keV X-rays and spatial resolution characterisation for PETAL diagnostics*, Rev. Sci. Instrum. **87** (2016) 043108

[32] http://www.srim.org/.

[33] http://www.comsol.com/.

[34] A. Macchi et al., *Ion acceleration by superintense laser-plasma interaction*, Rev. Mod. Phys. **85** (2013) 751.

[35] R.F. Schneider et al., *Resolution of the Thomson spectrometer*, J. Appl. Phys. **57** (1985) 1.

[36] T. Bonnet et al., *Response functions of imaging plates to photons, electrons and ^{4}He particles*, Rev. Sci. Instr. **84** (2013) 103510.

2016 JINST 11 C05010